

FARO tests corium-melt cooling in water pool: Roles of melt superheat and sintering in sediment



Gisuk Hwang^a, Massoud Kaviani^{b,c}, Kiyofumi Moriyama^c, Hyun Sun Park^{c,*}, Byoungcheol Hwang^c, Mooneon Lee^c, Eunho Kim^c, Jin Ho Park^c, Yahya Nasersharifi^a

^a Department of Mechanical Engineering, Wichita State University, Wichita, KS 67260, United States

^b Department of Mechanical Engineering, University of Michigan, Ann Arbor, MI 48109, United States

^c Division of Advance Nuclear Engineering, POSTECH, Pohang, Gyeongbuk 790-784, Republic of Korea

HIGHLIGHTS

- The numerical approach for FARO experimental data is suggested.
- The cooling mechanism of ex-vessel corium is suggested.
- The predicted minimum pool depth for no cake formation is suggested.

ARTICLE INFO

Article history:

Received 1 December 2015

Received in revised form 9 May 2016

Accepted 16 May 2016

JEL classification:

K. Thermal Hydraulics

ABSTRACT

The FARO tests have aimed at understanding an important severe accident mitigation action in a light water reactor when the accident progresses from the reactor pressure vessel boundary. These tests have aimed to measure the coolability of a molten core material (corium) gravity dispersed as jet into a water pool, quantifying the loose particle diameter distribution and fraction converted to cake under range of initial melt superheat and pool temperature and depth. Under complete hydrodynamic breakup of corium and consequent sedimentation in the pool, the initially superheated corium can result in debris bed consisting of discrete solid particles (loose debris) and/or a solid cake at the bottom of the pool. The success of the debris bed coolability requires cooling of the cake, and this is controlled by the large internal resistance. We postulate that the corium cake forms when there is a remelting part in the sediment. We show that even though a solid shell forms around the melt particles transiting in the water pool due to film-boiling heat transfer, the superheated melt allows remelting of the large particles in the sediment (depending on the water temperature and the transit time) using the COOLAP (Coolability Analysis with Parametric fuel-coolant interaction models) code. With this remelting and its liquid-phase sintering of the non-remelted particles, we predict the fraction of the melt particles converting to a cake through liquid sintering. Our predictions are in good agreement with the existing results of the FARO experiments. We address only those experiments with pool depths sufficient/exceeding the length required for complete breakup of the molten jet. Our analysis of the fate of molten corium aimed at devising the effective scenarios for its safe cooling in the containment so that predicted the minimum pool depth for no cake formation as functions of the melt superheat and water (subcooled/saturation) temperatures.

© 2016 Elsevier B.V. All rights reserved.

1. Introduction

One of the challenging consequences of light water reactor nuclear power plant accident is melting of the fuel and supporting structures followed by the movement of the molten material

(corium) into a water pool either inside or outside of the reactor vessel (Bürger et al., 2010; Magallon, 2006; Spencer et al., 1994). The interaction of the melt with the water pool is called the fuel-coolant interactions (FCIs), and it can be either in the energetic mode, i.e., steam explosion, or the non-energetic mode in which the breakup of the corium melt into small particles $d_p \sim 1\text{--}10\text{ mm}$ is expected. The latter is favorable for the molten core cooling and stabilization. The melt flowing into the water pool is

* Corresponding author. Fax: +82 54 279 9559.

E-mail address: hejsunny@postech.ac.kr (H.S. Park).

cooling is predicted using the empirical jet breakup/melt particle statistics, adjusted boiling heat transfer coefficient, particle trajectory treatments, separation of the loose-particle bed and cake, and cooling of the cake including heat transfer to the bottom collector plate. Since some of the aforementioned parameters are currently unknown, our parametric studies are based on the FARO test (Magallon, 2006). The predicted results are compared with the reported FARO test results (Magallon, 2006), and the possible detailed mechanisms are discussed and the parametric studies are also shown. We consider those FARO tests with the complete

breakup of molten jet, so can also predict the case of no-cake formation. In addition, for the ex-vessel severe accident mitigation, the Severe Accident Management Guideline (SAMG) often suggests to flood the cavity to provide sufficient cooling water to the relocated corium. We examined the potential of the model to investigate the effect of the water pool length on the corium coolability in terms of evaluating the minimum pool length of no cake formation.

2. Modeling particle-transit and cake-formation/cooling

To simulate corium-coolant interactions and corium coolability, the melt jet/particles and their fate has been experimentally studied, for example, in FARO tests (Magallon, 2006). The detailed fate of the melt particles during the particle transit in the FARO tests is shown in Fig. 1. In the experiment, (a) the superheated-melt jet pours into the water pool through a nozzle with the jet diameter, D_j , followed by jet breakup into the melt droplets (particles) over the jet breakup length, L_b , (b) the melt droplets transit by the gravity in the water pool, while cooled by film boiling and radiation, resulting in a solid shell formation (partial cooling), and (c) the partially-cooled droplets may remelt, which result in liquid-phase sintering and a cake formation (namely, remelting of large particles and liquid-phase sintered cake). Based on the aforementioned descriptions of the observation from the experiments, a physical model of the fate of the corium melt is developed as shown in Fig. 2. The three distinct periods shown in the figure, the particle-transit and the bed-formation, the remelt-wicking, and the cooling periods, are described below.

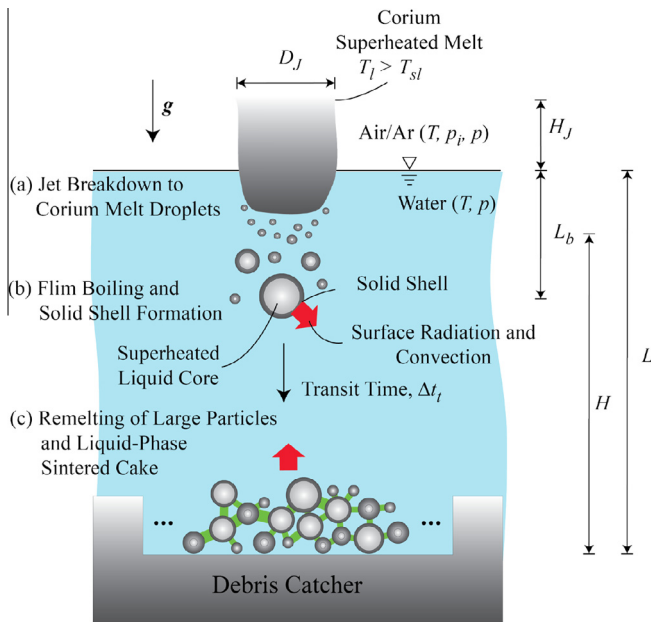


Fig. 1. Rendering/physical model of superheated corium melt during/after particle-transit period in the water pool, per FARO tests [1]. (a) Jet breakup forming corium melt droplets, (b) film boiling and solid shell formation, and (c) remelting of large particles and liquid-phase sintered cake. Water pool height, L , and jet breakup length, L_b , and effective particle-transit height, H , melt jet diameter, D_j , and melt jet transit height, H_j , are also shown.

2.1. Particle-transit period, Δt_t , and bed-formation period, Δt_{bed}

The particle-transit period is the travel time, starting from the corium melt jet entering the pool till it reaches the pool bottom, i.e., the particle-transit length is the same as the water pool length [(a) above]. In this period, the thermal-hydraulics of superheated melt jet breaks into droplets and transit in a saturated/subcooled water pool. The gravity jet completely breaks up in length, L_b , which primarily depends on the jet diameter, melt/water densities and the jet velocity, and may be affected by the melt surface tension, melt superheat, pressure (water subcooling and vapor den-

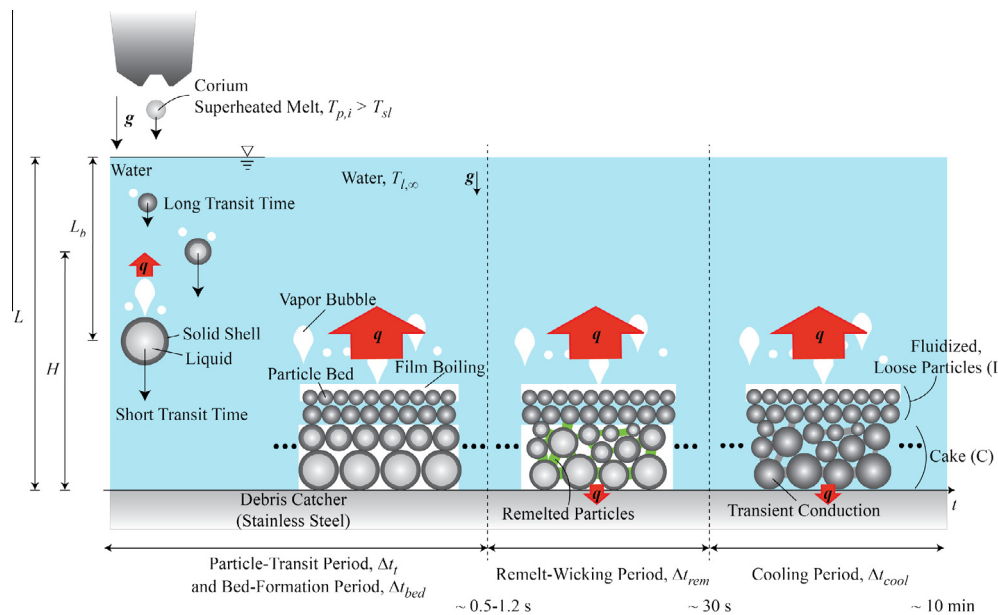


Fig. 2. Modeling/presentation of the fate of superheated corium melt during particle-transit and bed-formation Δt_{bed} , remelt-wicking Δt_{rem} , and cooling Δt_{cool} , periods.

sity), etc. (Bürger, 2006; Bürger et al., 1995; Moriyama et al., 2005). Incomplete breakup of the jet makes the analysis even more challenging. Since jet/droplets cool by film boiling, the upward bubbly/churn flows counter to the particle path cause the particle to meander, and also subcooled boiling may have local explosive or pulsation interactions that modify the particle sizes and movements (Chen et al., 1999; Kondo et al., 1995; Liu and Theofanous, 1996; Moriyama et al., 2005). The particle-size dependent viscous or inertial-drag/gravity force ratio results in size-dependent transit time. Here based on experimental observations, we develop models which are tractable and yet make relatively accurate predictions. The large particles have a short transit time, reaching the debris catcher faster, forming a stratified sediment. The excess heat (melt superheat) remaining during the short transit time would allow for the remelting of the large particles in the sediment. At the end of this period, there can be both loose (completely solidified) and remelt/sintered (cake) particles.

2.2. Remelt-wicking period, Δt_{rem}

Some of the large particles at the pool bottom can remelt due to remaining excess sensible and latent energy (caused by short particle transit time). In this period, the remelted particles capillary-percolate into the interparticle pores, resulting in liquid-phase sintering (German et al., 2009; German, 1985) and cake formation. A small mass fraction of the remelted particles can form large cake volume, by “binding” the neighboring solid particles with a residual melt bridge (as small as a few percent of the total volume) (German et al., 2009; German, 1985). Later, this mixture of the solid and remelted particles solidifies upon further cooling. This mixture of the solid and remelted particles leads to a non-uniform enthalpy distribution within the cake. Due to the different phases and particle size distributions, we treat the cake as a homogeneous medium having an equivalent total energy, since the percolation of the remelt particles is expected to homogenize the energy distribution. The cake is formed at the pool bottom, and below the loose particles. The cake contains the particles with the shorter transit time, while the smaller particles having larger transient time precipitate on its top (loose particle bed). The loose particle can also move by the boiling agitation. Note that if the pool length is too short to break up the melt jet, the initially molten jet could directly reach the bottom of the water pool, and it could percolate into the pores among the loose particle bed. However, there is no direct observation of this phenomenon and it is very challenging to distinguish between the remelt-driven and initially-molten-driven cake formations. Here, we focus on the remelt-driven cake formations, while modeling the experimental cases L-28 and L-31 with the complete jet breakup for the minimal initially-molten-driven cake formation.

2.3. Cooling period, Δt_{cool}

The cake and loose-particle beds have excess heat (especially the cake) and cool down through pool boiling from their top and bottom surfaces. In the cake bed, the local transient heat transfer is dominated by its low thermal conductivity (low thermal corium conductivity and high porosity), while remaining dry until it cools down to close to the water pool saturation temperature for the water to penetrate the cake for the efficient two-phase cooling. The loose particle bed is most likely well mixed with the two-phase water (film boiling) since it is assumed that the particles are free to move (fluidized bed), where tends to have a very large effective thermal conductivity. Note that the small particles most likely form a significant solid shell (Figs. 1 and 2) due to the efficient coolability during the water transit, and the particles tend to be free to move. Then, we assume that they can fluidize under

the boiling from the cake or interface between the cake and loose particle beds. This last period is designated as “long-term cooling period”, Δt_{cool} cooling.

Based on this physical model, the mathematical treatments of the hydrodynamic and thermal aspects are discussed below.

3. Analyses

3.1. Hydrodynamic model: particle transit period

The particle-size-dependent transit time is calculated using the force balance among the drag, F_D , the buoyancy, F_B , and the gravity, F_g , as shown in Fig. 3, and it is given as (Munson et al., 2012)

$$F_D = -\frac{1}{2}C_D\rho_l A v_p^2, F_B = -\rho_l g V_p, \text{ and } F_g = \rho_p g V_p, \quad (1)$$

where C_D is the drag coefficient, A is the particle cross-sectional area, v_p is the particle velocity, ρ_l is the liquid water density, ρ_p is the particle density, V_p is the particle volume, and g is the gravitational acceleration. Since the corium droplet (particle) is cooled by the film boiling, C_D is calculated using the water vapor properties as (Munson et al., 2012; Vakarelski et al., 2014)

$$C_D = \max(24/Re_{d_p}, 18.5/Re_{d_p}^{0.6}, 0.44), \quad (2)$$

where

$$Re_{d_p} = \frac{\rho_v d_p v_p}{\mu_v}, \quad (3)$$

where μ_v is the water vapor viscosity and d_p is the particle diameter. Note that the v_p is particle-size dependent, and the Eqs. (1)–(3) were solved iteratively.

The equation of the motion becomes

$$0 = F_D + F_B + F_g, 0 = -\frac{1}{2}C_D\rho_l A v_p + (\rho_p - \rho_l)gV_p. \quad (4)$$

The predicted particle transit period $\Delta t'_t$ for the pool height L (Fig. 2), is shown in Fig. 4(a) and (b), for both L-28 and L-31 tests (see Tables 1 and 2 for the details on the parameters used). Note that the exact predictions for the particle transit periods requires the corium material composition, geometries, and relevant thermos-physical properties, which are currently unavailable, and here we used the simple approach based on the spherical geometry for the corium particle, without losing a generality.

This period will be modified to include the jet breakup length and realistic two-phase hydrodynamic model below.

(a) Particle-size distribution

The particle diameter is between the 0.25 and 15 mm, based on the FARO tests (Magallon, 2006). The particle diameter distribution

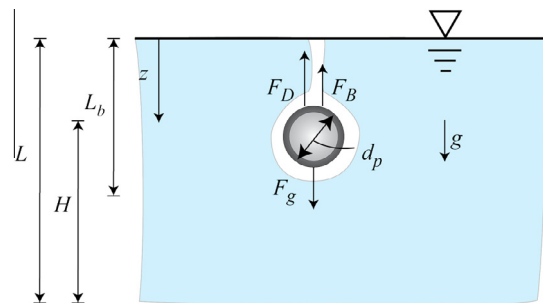


Fig. 3. Rendering of various forces acting on the melt particle during transit in water pool. The parameters used in analysis including the physical water pool height, L , jet breakup length, L_b , and effective water pool height, H , are also shown.

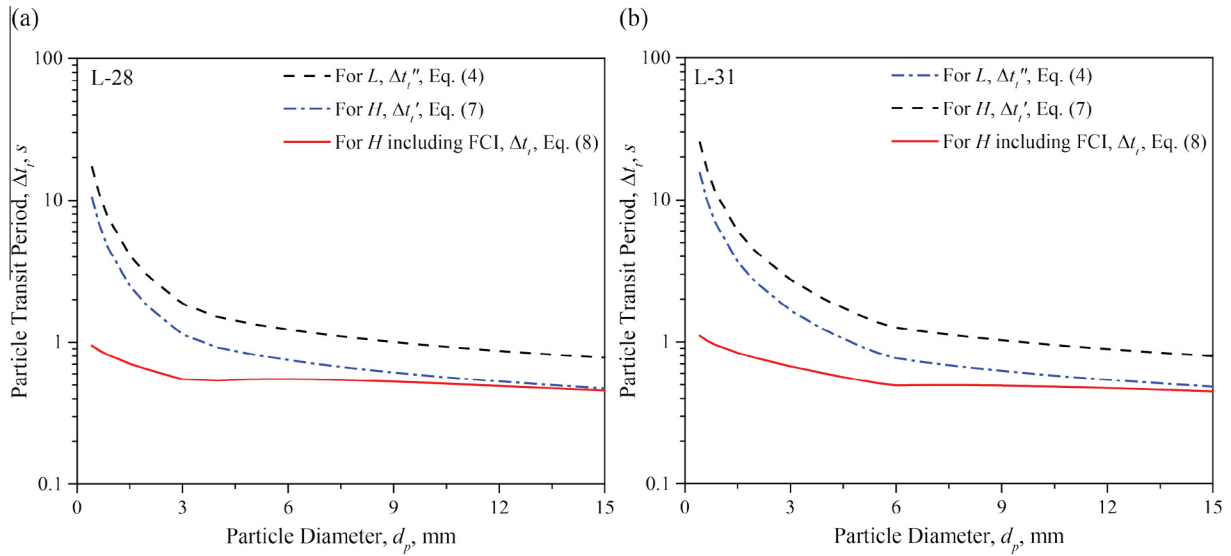


Fig. 4. Variations of predicted particle-transit period, Δt_p (Eq. (8)) as a function of particle diameter, d_p , for experiments (a) L-28 and (b) L-31. The predicted particle-transit period, $\Delta t'_p$ (Eq. (4)) for the stationary water pool with the physical water pool height, L , and the effective-water-pool-height-adjusted, particle-transit period $\Delta t'_p$ (Eq. (7)) with the effective water pool height, H are also shown.

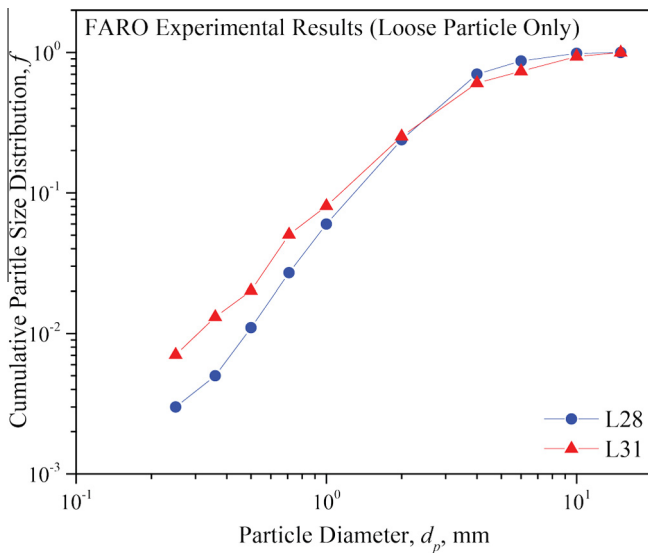


Fig. 5. Variations of measured cumulative particle size distribution with respect to the particle diameter, d_p , for experiments L-28 and L-31 (Magallon, 2006). The results are for the loose particles only.

of the initial melt jet is crucial to hydrodynamic and heat transfer models, i.e., the prediction of the transit time and the energy distribution within the cake during its cooling period. However, due to the complex jet breakup phenomena and limited in-situ particle distribution measurement techniques, the diameter distribution for only the loose particle is measured after the long-term cooling period as shown in Fig. 5, for both beds (Magallon, 2006). In this study, we assume that the initial particle diameter distribution is the same as the loose particle diameter distribution (due to lack of experimental data).

(b) Jet breakup

We assume that the melt jet completely breaks up after the jet breakup length L_b . We used a correlation for the jet breakup length proposed by Moriyama et al. (2005). Based on various experimen-

tal data including those of FARO [2], PREMIX (Kaiser et al., 2001) and themselves, they divided two regimes of the jet breakup length depending on the Bond number with the jet diameter

$$Bo_j = \frac{\rho_m g D_{ji}^2}{\sigma_m}, \quad (5)$$

where ρ_m is the melt density, D_{ji} is the melt jet diameter, and σ_m is the melt surface tension, and they showed the breakup length for large jets, i.e. $Bo_j > 50$, including FARO L-28 and 31 ($Bo_j \sim 200$), agrees with the Taylor-type correlation

$$\frac{L_b}{D_{ji}} = C_J N_\rho^{1/2}, \quad (6)$$

where $N_\rho = \rho_p / \rho_l$, and ρ_l is the liquid water density, and $C_J = 10$. In some FARO test cases, the pool height, L , is smaller than L_b , i.e., some of the melt jet directly reaches the debris catcher. In these cases, there can be a sunken melt cake in addition to liquid-phase sintered cake. Since the physical features of these two cakes may not be clearly distinguishable, here, we consider only the tests where the water pool depth is large enough to completely breakup the jet, i.e., $L > L_b$, i.e., FARO tests L-28 and L-31 (Magallon, 2006). Due to the continuous jet breakup phenomena, it is very challenging to predict the exact particle-transit length. Here, we use a geometric average approach

$$H = L - 0.5L_b, \quad (7)$$

where H is the effective particle transit length. The equation of the particle motion, Eq. (4), is numerically solved over the particle-transit period, $\Delta t'_p$, using H , and an iterative method.

(c) Local hydrodynamics

The particles falling in the water pool have initial velocities given when they are produced by the melt jet breakup, and are subject to interactions with the flow. To take those factors into account, we also introduce an empirical correction factor for the effective particle-transit time Δt_t , i.e.,

$$\Delta t_t = \beta \Delta t'_t, \quad (8)$$

where β is in turn

$$\beta = 1 - \exp(-\gamma d_p), \quad (9)$$

where $\gamma = 221 \text{ (m}^{-1}\text{)}$ for L-28 and $172 \text{ (m}^{-1}\text{)}$ for L-31 (Fig. 6), determined from simulations of fuel-coolant interaction (FCI) using

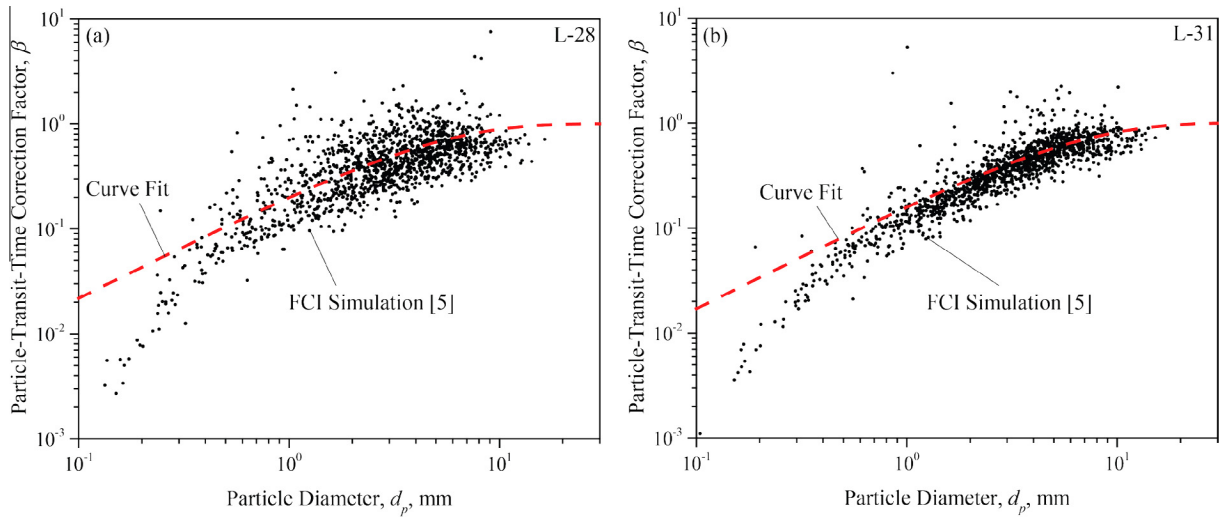


Fig. 6. Predicted variations of predicted particle-transit-time correction factor, β , with respect to the particle diameter d_p , is the from fuel-coolant interaction (FCI) simulations (Moriyama et al., 2015), (a) L-28, and (b) L-31. The curve fits are also shown.

JASMINE (Moriyama and Park, 2016). Their simulations include the empirical models for the local hydrodynamic interactions of the melt particles and the water two-phase flow, and the particle-size distribution. The predicted results indicate that the majority of the particles transit with velocities slightly larger than that in still water, due to the initial momentum after the separation from the continuous melt jet and interactions with the agitated water. Including the effective water pool height, and the correction factor, β , the predicted transit time is shown in Fig. 4(a) and (b) for both L-28 and L-31 cases. The correction factor, β , significantly reduces the particle transit time especially for the small particle diameter, while the effective transit height, H , and uniformly reduces it for all the particle diameters. The correction factor, β , overpredicts the small size particles, $d_p < 1$ mm, leading to longer particle transit time and larger (most likely sensible heat) particle thermal energy. However, this effect on the loose-particle bed is small, i.e., <5%.

3.2. Heat transfer model: particle transit and long-term cooling periods

3.2.1. Particle-transit period, Δt_t

During the particle-transit period, the superheated melt ($T > T_{sl}$) results in the significant radiation during the film boiling, which solidifies the particles. The transient radial temperature distribution within the particles including the melt/solid interface is calculated using the 1-D, explicit heat transfer numerical analysis as shown in Fig. 7.

The energy equation is (Kaviany, 2011)

$$\nabla \cdot \mathbf{q} = -\rho c_p \frac{\partial T}{\partial t} + \dot{s}, \quad \mathbf{q} = -k \nabla T, \quad (10)$$

where ρ is the density, c_p is the specific heat, t is the cooling time, \mathbf{q} is the heat flux vector, k is the thermal conductivity, T is the temperature, and \dot{s} is the liquid–solid phase-change thermal energy generation rate. Under 1-D heat transport in the radial direction only, this becomes (Kaviany, 2011)

$$\rho c_p \frac{\partial T}{\partial t} = \frac{k}{r^2} \left[\frac{\partial}{\partial r} \left(r^2 \frac{\partial T}{\partial r} \right) \right] + \dot{s}, \quad (11)$$

where α is the thermal diffusivity, and r is the radial coordinate. The phase change front is calculated using the enthalpy method. At the boundary of $r = 0$, the temperature distribution is symmetric, and it

is calculated using the following relation (Maclaurin expansion at the origin) (Poulikakos, 1994)

$$\frac{\partial T}{\partial t} = 3\alpha \frac{\partial^2 T}{\partial r^2}. \quad (12)$$

At $r = r_p$, we have

$$-k \frac{\partial T}{\partial r} \Big|_{r=r_p} = q, \quad (13)$$

where, q is the heat flux to the water pool by the radiation and film boiling as given as (Liu and Theofanous, 1995)

$$q = q_{fb} + \frac{7}{8} q_r, \quad (14)$$

where q_{fb} is the film-boiling heat flux and q_r is the radiative heat transfer. For radiation (Kaviany, 2011), we select the emissivity $\varepsilon_r = 0.8$ (Salikhov et al., 1999) and as mentioned view factor $F = 0.1–0.7$, as a fitting parameter.

The temperature distribution is discontinuous near the phase change temperature, and this is calculated using the enthalpy

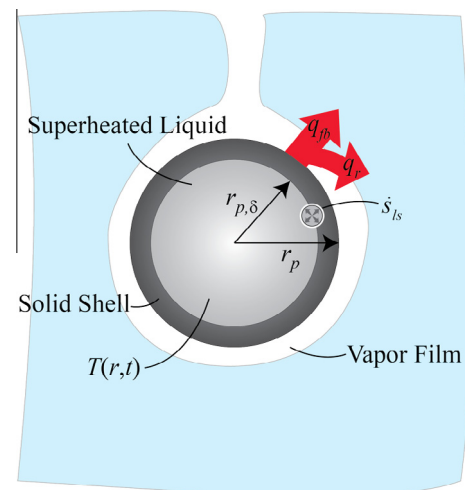


Fig. 7. Rendering of liquid melt (particle) and its solid shell formed upon cooling in water. The film boiling–radiation heat flux, phase change, and water vapor film are also shown.

method given in the previous study (Voller and Cross, 1981) with Eq. (11) written as

$$\frac{\partial h}{\partial t} = \frac{\alpha}{r^2} \left[\frac{\partial}{\partial r} \left(r^2 \frac{\partial T}{\partial r} \right) \right], \quad (15)$$

$$h = \begin{cases} c_p T, & T < T_{sl} \\ c_p T_{sl} + \Delta h_{sl}/2, & T = T_{sl} \\ \Delta h_{sl} + c_p (T - T_{sl}), & T > T_{sl} \end{cases} \quad (16)$$

where T_{sl} is the solid-liquid phase change temperature, and Δh_{sl} is the enthalpy of fusion. Then Eq. (15) is solved with explicit finite difference method. In fact, Eq. (15) is the discontinuous function, which may result in the numerical instabilities and/or unphysical predictions. The adjusted time step is used to address the challenges (Voller and Cross, 1981). Then, temperature is determined from

$$T = \begin{cases} h/c_p, & h \leq c_p T_{sl} \\ T_{sl}, & c_p T_{sl} \leq h \leq c_p T_{sl} + \Delta h_{sl} \\ (h - \Delta h_{sl})/c_p, & h > c_p T_{sl} + \Delta h_{sl}. \end{cases} \quad (17)$$

3.2.2. Remelting period, Δt_{rem}

The particle-transit time increases as the particle size decreases. This yields the probable sediment scenario that the larger particles accumulate at the bottom, whereas the smaller particles deposit in the top. Also, the larger particles have larger superheat content due to the shorter particle-transit time and smaller surface/volume ratio, and the solid shell can remelt. For the particle remelt criteria, the excess specific enthalpy is predicted using the following relation,

$$\Delta h_{ex}^* = \frac{\frac{1}{V} \int_V h dV}{c_p T_{sl} + \Delta h_{sl}}, \quad (18)$$

where V is the particle volume, h is the enthalpy of the particle, c_p is the specific heat of the particle, T_{sl} is the melting temperature, and Δh_{sl} is the heat of fusion, and for $\Delta h_{ex}^* > 1$, the particle remelts. Note that the radioactive decay is not considered here since it aims at modeling the FARO tests.

To form the cake, only a fraction of the particles need to remelt, and this phenomenon is known as the liquid sintering (German et al., 2009; German, 1985). The remelted particles (liquid phase) spread through the solid particle by capillary suction in a short time and we assume uniform spread through the cake. The exact treatment requires the capillary pressure, permeability, etc., but here, we use an empirical treatment.

The required minimum pool length for no cake formation, L_o , is the pool length results with zero excessive enthalpy of the largest particle size (15 mm), after the particle transit, i.e., $\Delta h_{ex}^* < 1$ for $d_p = 15$ mm, since the largest particle remelts first.

3.2.3. Cooling period, Δt_{cool}

For the (long-term) cooling period, there are four main physical/mathematical domains, namely, water pool, loose particle (LP), cake (C) bed, and debris catcher (DC), as shown in Fig. 8.

(a) Water pool

Due to the large superheat of the loose-particle and cake bed and the pool boiling prevails at the top surface of the loose-particle bed, and the pool boiling correlation for the plain surface is used between the loose particle bed and water pool because of the lack of a better alternative (Nukiyama, 1966).

(b) Loose-particle bed

The loose particles are assumed to be free to move, i.e., no adhesion to neighbors, and the heat transfer mechanism within the bed

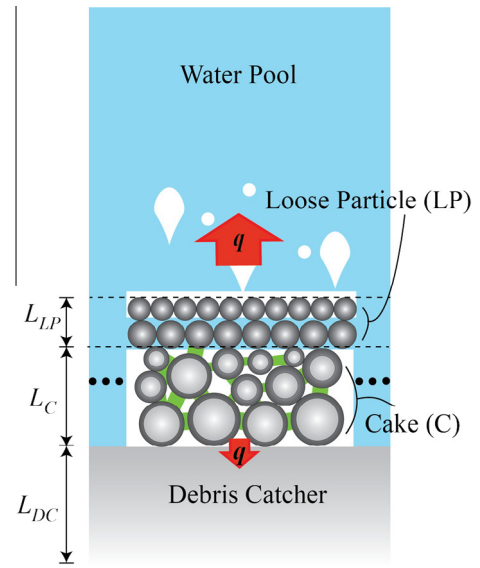


Fig. 8. Presentation of the loose particle (LP) and cake (C) cooling, showing the surrounding water pool, debris catcher (DC), heat transfer from top and bottom, and dimensions.

is poorly understood since the thermal-hydraulic behaviors of the loose particles under the pool boiling varies from the granular to the fluidized bed treatments, depending on the degree of the dynamic motions of the particles and water (Kaviany, 2001). We expect this moving bed of water liquid/vapor and particles to have a nearly uniform temperature distribution, i.e., very large effective thermal conductivity. We use volume averaging over the bed volume V , i.e.,

$$\langle \varphi \rangle = \frac{1}{V} \int_V \varphi dV, \quad (19)$$

where φ is a thermophysical quantity (e.g., h , ρ , c_p) (Oliveira and Kaviany, 1999). This includes all particles (inner melt and solid outer shell which eventually occupies the entire particle). We use saturated water properties and a porosity $\varepsilon_p = 0.5$ (same as that used for the cake). Although the exact heat transfer coefficient between the loose particles and boiling water (inside the bed) is complex, we assume it is an order of magnitude smaller compared to the pool boiling on plain surface (due to hindrance in bubble escape).

(c) Cake bed

The temperature distribution within the cake is predicted using the volume-averaged treatment with the remelt particles, liquid sintering, and eventual solidification. The liquid melt uniformly spreads and we assume uniform properties. The energy equation is [similar to Eq. (15), but for vertical direction, z],

$$\frac{\partial \langle h \rangle}{\partial t} = \frac{\langle k \rangle}{\langle \rho \rangle} \frac{\partial^2 \langle T \rangle}{\partial z^2}, \quad (20)$$

where $\langle \rangle$ represents the local volume average. During the initial high-temperature history, ~ 3000 K, radiation heat transfer through the pores dominates. While later the solid-matrix conduction dominates. The cake effective thermal conductivity is

$$\langle k \rangle = \langle k_s \rangle + \langle k_r \rangle \quad (21)$$

where $\langle k_r \rangle$ is the radiant thermal conductivity for porous medium (Kaviany, 1995), and the mean (loose) particle diameter is used to calculate $\langle k_r \rangle$, and $\langle k_s \rangle$ is the effective thermal conductivity in the cake (porous medium), and $\langle k_s \rangle = (1 - \varepsilon_c)k_s + \varepsilon_c k_v$, k_s is the

corium melt thermal conductivity, taken as $k_s = 2.88$ W/m-K at 3000 K [cite], and k_g is for the water vapor (negligible contribution) and the cake porosity is taken as $\varepsilon_c = 0.5$. Temperature dependent solid thermal conductivity is used.

Since the cake temperature remains high (large vapor pressure within the cake) after the particle transit period, the cake remain dry until the cake cools down to near the water pool saturation temperature. Then, water can penetrate the cake and evaporate within it (Udell, 1985). Once the water penetrates, the evaporation front moves into the cake for the efficient evaporation cooling (heat pipe effect). The onset of the water penetration is guided by the critical heat flux of the deep porous coating (Udell, 1985)

$$\frac{q_{CHF,cake}}{K \rho_g \Delta h_{lg} g (\rho_l - \rho_g) \left[1 + \left(\frac{\rho_l \mu_g}{\rho_g \mu_l} \right)^{\frac{1}{4}} \right]^{-4}} = 1. \quad (22)$$

We assume a cake permeability of $K = 10^{-11}$ m² and this give a $q_{CHF,cake} = 3.3 \times 10^4$ W/m² for L-28. Indeed, the onset of the water penetration is expected to begin at the cake temperature of nearly the same as the water pool saturation temperature, but given uncertainty of the permeability of the cake, it may not be realistic prediction. Here, we postulate that the water begins to penetrate the cake when it cools to 50 K above the water pool saturation temperature (an estimation of the cake superheat upper limit for water penetration). For the evaporation cooling, we use the additional results from the previous study on the effective evaporative thermal conductivity $\langle k \rangle_{lg} = 700$ W/m-K (Udell, 1985). This heat-pipe conductivity effectively cools the cake during the last stage of cooling. Alternatively, the cake cooling can be treated as a liquid penetration front, opposite to the drying problem (Rogers and Kaviany, 1992).

(d) Debris catcher

At the bottom of the pool, the particles are collected by a stainless steel debris catcher (Fig. 2). The catcher is a shallow bucket, with internal 2-D heat transfer in radial and vertical directions. Here we use a 1-D conduction along its thickness, but increase the surface area to the pool boiling to include the radial heat spread. The transient, distributed temperature is predicted using Eq. (20), and we will compare the predicted catcher/cake interface temperature with the experimental results to validate this model (Magallon, 2006).

3.2.4. Boundary/interface conditions

There are three (L-31)/four boundary/interface (L-28) conditions that need to be considered in the numerical analysis, namely, loose-particle-bed/pool, cake/loose-particle-bed, catcher/cake, and pool/catcher.

(a) Loose particle bed/pool

At the interface between the loose-particle bed and the water pool, there is boiling (including bubbles from within the loose-particle bed) and we expect the bubble agitation to move of the loose particles. We use the pool-boiling correlations for plain surface (Lienhard, 2013).

(b) Cake/loose-particle-bed

There is also pool boiling at interface of cake and loose particle bed, and we again use the pool-boiling correlation for plain surface, for lack of more accurate treatments (Lienhard, 2013).

(c) Catcher/cake

Between the cake and catcher, there is a thermal contact resistance, which in general depends on thermal contact pressure, surface condition, pair-material properties, etc. We use thermal contact resistance $AR_{k,c} = 0.5 \times 10^{-3}$ K/(W/m²) for L-28, and 10^{-3} K/(W/m²) for L-31, assuming better contact with catcher for L-28 (Schneider, 1985).

(d) Pool/catcher

The top surface of catcher is submerged in the pool and its bottom surface is also exposed to water so it is subject to downward facing pool boiling. The lower surface would have some resistance to its liquid supply and also vapor escape. So we triple the thermal resistance of the pool boiling (Lienhard, 2013) for the catcher lower surface.

4. Results and discussions

4.1. Particle-transit period

Using Eq. (8), the predicted particle-transit times as a function of the particle diameter are shown in Fig. 4 for L-28 and 31 cases. This time period decreases with increasing particle diameter due to the smaller viscous-drag to gravity-driven force ratio. For small particle diameters, $d_p < 3$ mm for L-28 and $d_p < 6$ mm for L-31, the particle-transit period exponentially decreases, while for larger

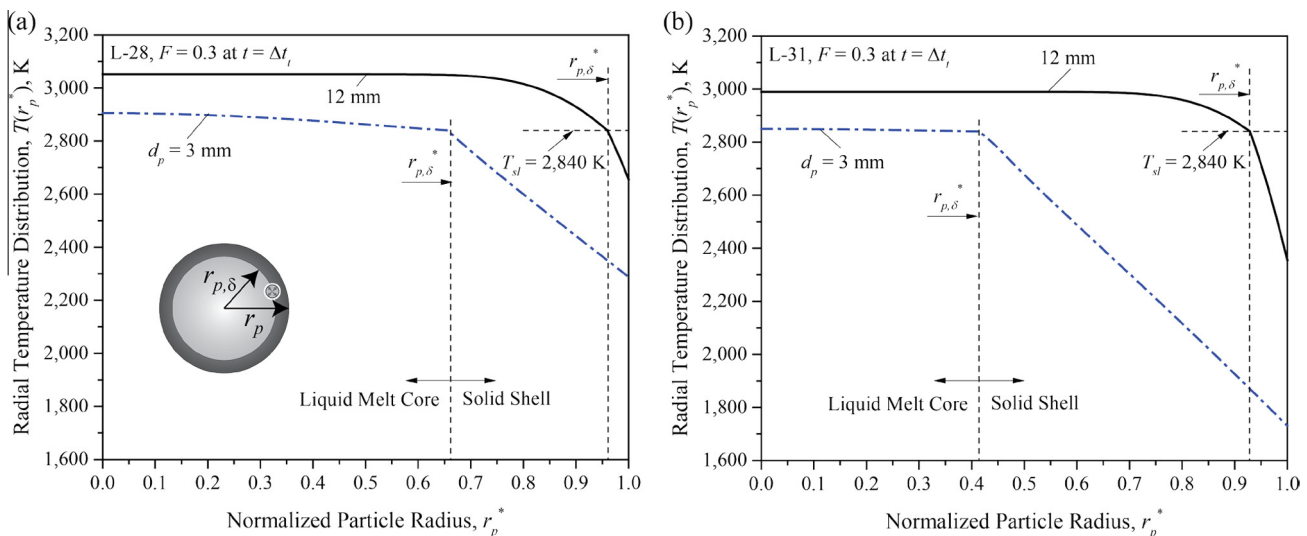


Fig. 9. Predicted radial temperature distributions at the end of the particle-transit period, for (a) L-28 and (b) L-31, as a function of normalized particle radius, $r^* = r/r_p$, for $r_p = 3$, and 12 mm, with $F = 0.3$. The melting temperature, $T_{sl} = 2840$ K and the normalized melt radius location, $r_s^* = r_p \delta / r_p$ [inset in (a)], are also shown.

particle diameters, $d_p > 3$ mm for L-28 and $d_p > 6$ mm for L-31, it slowly decreases as the viscous-drag force overcomes the buoyant force. The difference between the L-28 and L-31 tests are due to the pool and initial melt temperatures. These predicted results are used in the particle temperature distributions and excess enthalpy predictions which are in turn used in the long-term cooling predictions.

4.2. Radial temperature distribution of particles after particle-transit period

The radial temperature distribution and location of the solid/melt interface play significant roles in the coolability and excess specific enthalpy/particle remelt, especially for the large particles. The solid/melt interface depends on the particle size, initial melt superheat, particle-transit time, and view factor. The transient temperature distribution in each particle is predicted (including the solidification) using Eqs. (15)–(17), particle size distributions

(Fig. 5), and view factor ($F = 0.1, 0.3, 0.5,$ and 0.7). The temperature distributions for $r_p = 3$ and 12 mm, L-28 and L-31 tests with view factor $F = 0.3$, as a function of the normalized particle radius, $r_p^* = r/r_p$, are shown in Fig. 9(a) and (b). Since the heat removal from the particle surface is dominated by film boiling and radiation, the minimum temperature occurs at the surface, while the maximum temperature is at the center of the particle, $r_p = 0$, with temperature gradient of zero due to symmetry. The smaller particle, $d_p = 3$ mm cools more effectively compared to larger, $d_p = 12$ mm, as the volume-to-surface ratio is small resulting in small temperature variations and smaller melt radius, $r_{p,\delta}^*$. The larger particle cools only near the surface while its core remains unchanged for $r_p^* < 0.8$. The cooling in the L-28 test is prolonged compared L-31, since the initial melt and pool temperatures are larger for L-31 (under similar particle-transit time), which in turn lead to larger melt radii.

The predicted, normalized melt radii, $r_{p,\delta}^*$, for L-28 and 31 test are shown in Fig. 10(a) and (b), as a function of the particle

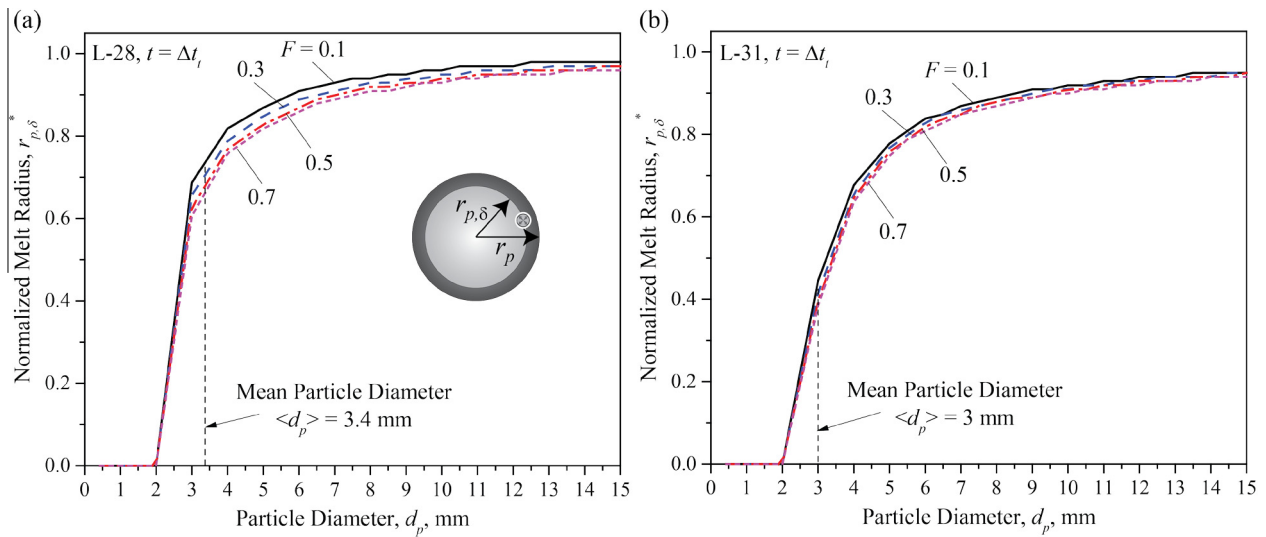


Fig. 10. Variations of predicted normalized melt/solid interface location ($r_{p,\delta}^* = r_p \delta / r_p$) with respect to particle diameter, for (a) L-28 and (b) L-31, for various view factors, $F = 0.1, 0.3, 0.5,$ and 0.7 . The mean particle size, $\langle d_p \rangle = 3.4$ mm for L-28 and 3.0 mm for L-31.

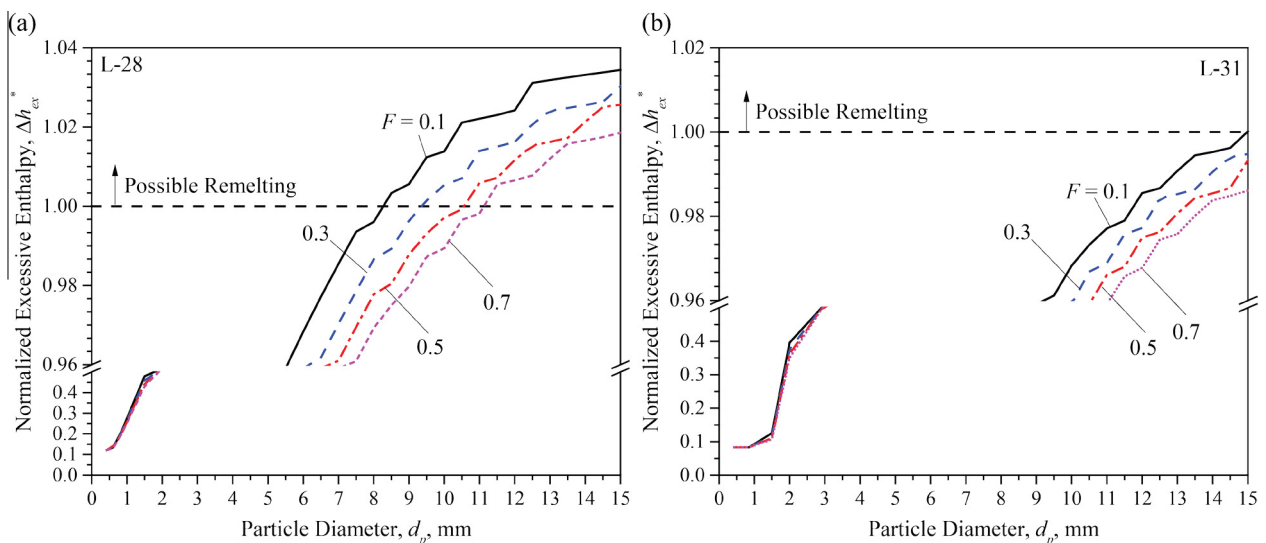


Fig. 11. Variations of predicted normalized excess specific enthalpy, Δh_{ex}^* as a function of the particle diameter, d_p , for (a) L-28 and (b) L-31 cases, for view factors, $F = 0.1, 0.3, 0.5,$ and 0.7 . The $\Delta h_{ex}^* > 1$ indicates possible remelting after the particle-transit period.

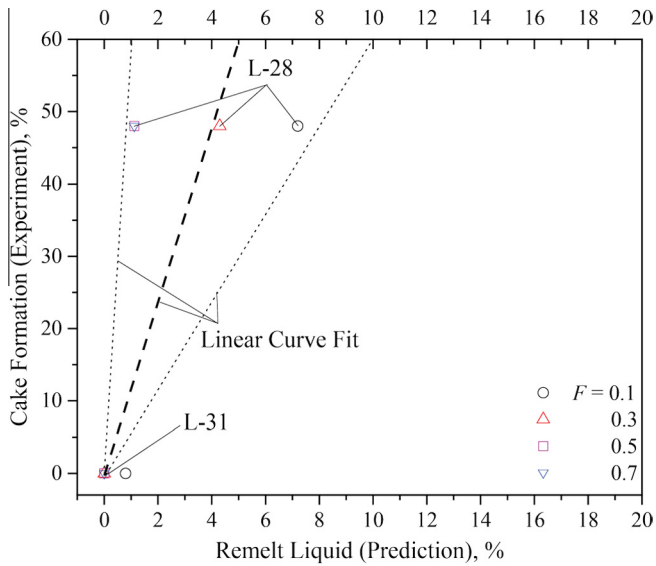


Fig. 12. Measured corium cake formed as percentage of corium (L-28 and L-31 (Magallon, 2006)) as a function of predicted liquid fraction for various view factors, $F = 0.1, 0.3, 0.5,$ and 0.7 . The suggested linear curve fit is also shown.

diameter, for various view factors F . As F increases, the normalized solid shell location decreases and the smaller particles diameter cool below the melting temperature (then form the loose particles), i.e., $r_{p,\delta}^* \sim 0$. For L-31, the particles cool significantly due to the large pool subcooling and lower initial melt temperature, resulting in smaller $r_{p,\delta}^*$ compared to L-28. Note that for L-31, the $r_{p,\delta}^*$ barely changes since film boiling is dominant over the radiation heat transfer.

The normalized excess enthalpy, Δh_{ex}^* , is predicted as a function of various view factor, $F = 0.1, 0.3, 0.5,$ and 0.7 , and particle diameters for L-28 and 31 cases as shown in Fig. 11(a) and (b). This determines the minimum particle diameter required for remelting, $d_{p,rem}$, for $\Delta h_{ex}^* > 1$. For the L-28 test, the smaller view factors, $F = 0.1$ and 0.3 , allow for the less-intense coolability, so smaller particle particles can remelt, whereas the larger view factor yields efficient cooling, so only larger particles remelt. For the L-31, the

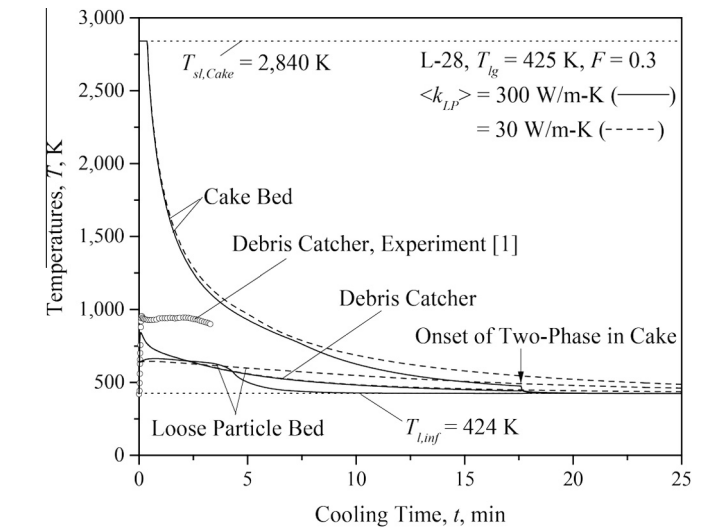
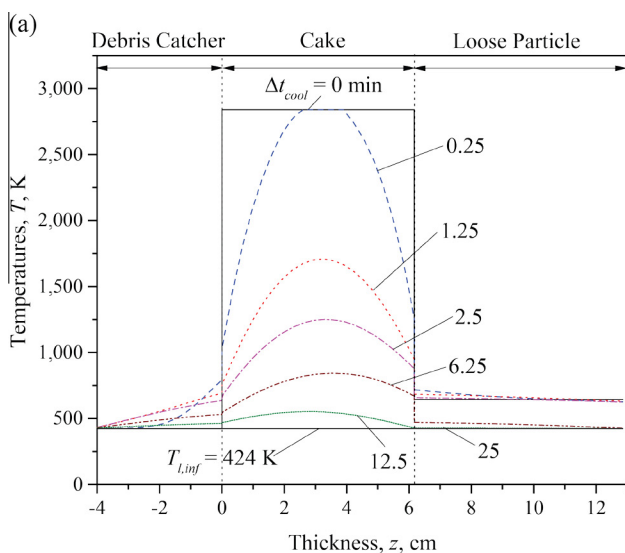


Fig. 14. Same as Fig. 13(a), with the effective thermal conductivity of the loose-particle bed, $\langle k_{LP} \rangle = 30$ and 300 W/m-K, representing granular and fluidized beds.

significant pool subcooling (film boiling) results in effective cooling, so there are only loose particles for all view factors.

4.3. Liquid sintering and cake formation

Using the minimum remelt particle diameter (Fig. 11), the melt mass fractions of the particles are predicted for several view factors, for L-28, and 31 tests, and shown in Fig. 12. Here, the 5/60 ratio reasonably fits the predicted melt to cake mass ratio, for $F = 0.3$. This view factor is used for the heat transfer model leading to the initial enthalpy (or temperature) distributions in the cake and loose-particle beds in the cooling history predictions.

4.4. Long-term cooling: cake, loose-particle beds, and debris catcher temperatures

The spatial and temporal temperature distributions of the cake and loose-particle beds, and the debris catcher are important in the

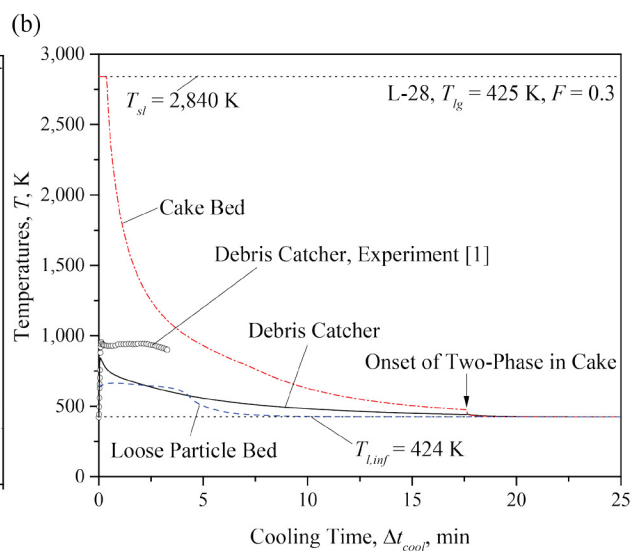


Fig. 13. (a) Predicted spatial temperature distributions of debris catcher, cake bed, and loose particle bed for several elapsed time since start of cooling period, for L-28. (b) Predicted temporal temperature variations of the debris catcher (interface with cake bed), cake bed (center) and loose particle (uniform temperature), for L-28. The predicted debris catcher temperature is compared with the experiment (Magallon, 2006). The water pool temperature and the onset of the two-phase in cake bed are also shown.

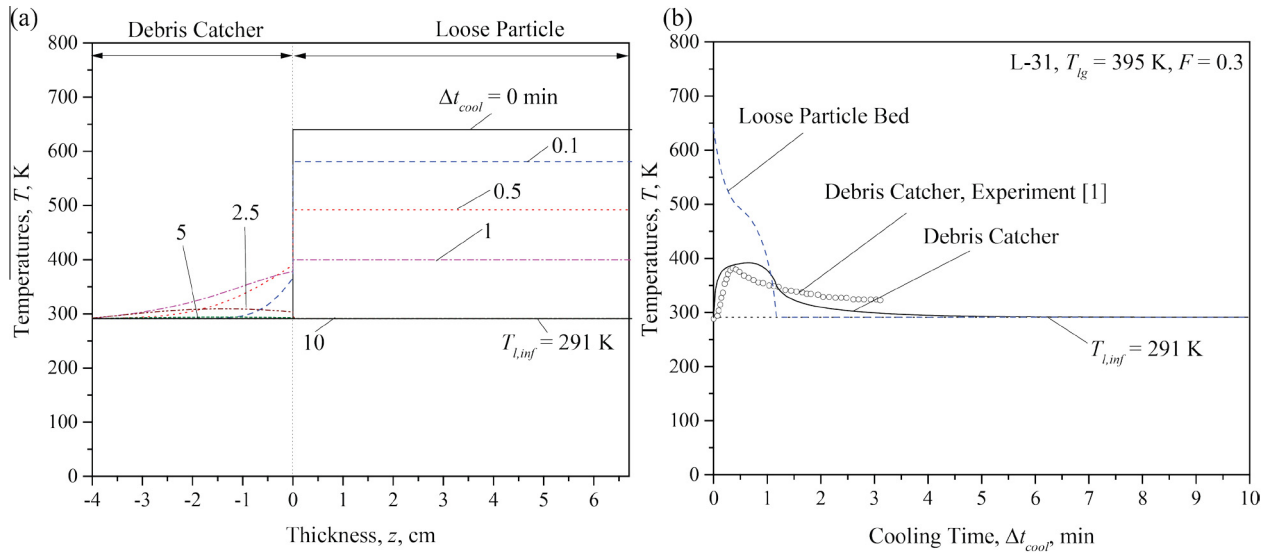


Fig. 15. Same as Fig. 13, but for L-31. Note that there is no cake bed.

nuclear safety analysis. We predict these temperature distributions for the L-28 and L-31 tests, and compare with the available experiment results (Magallon, 2006). The initial temperatures of the cake and loose particles are calculated based on the results at the end of the particle-transit period. The initial temperature of the catcher is the same as that of the water pool.

For the L-28 test, Fig. 13(a) shows the predicted, spatial temperature distributions for several cooling times in the debris catcher, cake and loose particle beds, while Fig. 13(b) shows the temperature history at the catcher/cake interface, cake-bed center, and loose-particle-bed center. At $\Delta t_{cool} = 0$, the cake has large superheat

and solidifies starting from the interfaces between the catcher/cake and cake/loose-particles (nearly symmetric). All completely cool down to the pool temperature in $\Delta t_{cool} \sim 18$ min. The cake remains dry resulting in boiling on its surfaces until it is cooled down to nearly 50 K above the pool saturation temperature at about $\Delta t_{cool} \sim 17.5$ min. After this, we expect water penetrates the cake and setting the heat-pipe effect. The initial loose-particle temperature is about 700 K and it cools down to the pool temperature within 6 min. The debris catcher temperature initially increases to 800 K, followed by the gradual cooling along with the cake. The predicted catcher temperature underestimates the experimental results, perhaps mainly due to uncertainty in the initial melt temperature. Further improvements can be made with improved particle-size distribution, thermal contact resistance, multidimensional heat spreading, etc. The predicted temperature distributions do not change significantly for $0.1 \leq F \leq 0.3$ (Fig. 11(a)), while these significantly change the remelt particle mass ratio (Fig. 12).

The treatment of the loose particles motion as granular or fluidized bed, can be tested relating the rigor of motion to an effective bed thermal conductivity. Here we use $\langle k_{LP} \rangle = 30$ for granular and 300 W/m-K for fluidized bed. The predicted temperature history of

Table 1
Summary of FARO experimental conditions for tests L-28 and L-31 (Magallon, 2006).

Case	Mean loose particle size $\langle d_p \rangle$, mm	Initial melt temperature, $T_{p,i}$, K	Water temperature, T_w , K	Water pool height, L , m	Corium cake formation, %
L-28	3.0	3052	424	1.44	48
L-31	3.4	2990	291	1.45	0

Table 2
Thermophysical properties used.

Parameter	Magnitude	Parameter	Magnitude
Water (at saturation temperature)		Cake (C)	
Liquid density, ρ_l , kg/m ³	917 (L-28), 943 (L-31)	Porosity, ϵ_C	0.5
Dynamic viscosity, μ , Pa-s	1.4056×10^{-5} (L-28), 1.3065×10^{-5} (L-31)	Thickness, L_C , m	0.0663 (L-28), 0.0 (L-31)
Specific heat, c_p , kJ/kg-K	4.22 (L-28), 4.18 (L-31)	Loose particle (LP)	
Saturation temperature, K	425 (L-28), 395 (L-31)	Porosity, ϵ_{LP}	0.5
Vapor density, ρ_v , kg/m ³	2.456 (L-28), 0.997 (L-31)	Thickness, L_{LP} , m	0.0622 (L-29), 0.0676 (L-31)
Melt particle		Debris catcher (DC)	
Density, ρ_p , kg/m ³	7960	Density, ρ_{DC} , kg/m ³	7900
Specific heat, c_p , J/kg-K	565	Specific heat, c_p , J/kg-K	530
Emissivity, ϵ_p	0.79	Thickness, L_{DC} , m	0.04
Heat of fusion, Δh_{sl}	3.62×10^5 kJ/kg-K	Thermal contact resistance, $AR_{k,c}$, K/(W/m ²)	0.5×10^{-3} (L-28) 1×10^{-3} (L-31)

various locations, for the L-28 test, are predicted as shown in Fig. 14 [otherwise same as Fig. 13(b)]. The results show the granular and fluidized approximations give similar predictions.

For the L-31 test, Fig. 15(a) shows the predicted temperature distributions at several cooling times for the catcher and loose particle bed, while Fig. 15(b) shows the predicted temperature history at the catcher/cake interface, and loose-particle bed center. After a short cooling time, i.e., ~5 min they all reaches the pool temperature. This shorter time is due to the lower initial melt temperature and significant water subcooling. The initial loose-particle bed temperature is about 650 K and cools down to the pool temperature within 1.2 min. The catcher temperature initially increases to 400 K, followed by the gradual cooling. The predicted temperature reasonably agrees the experimental results. Further improvements can be made with improved thermal contact resistance, boiling heat transfer relation for the catcher bottom surface, and multidimensional heat spread within the catcher. (See Tables 1 and 2).

4.5. Minimum pool depth for no cake formation, L_o

The variations of the predicted minimum pool depth, as a function of the initial melt superheat $\Delta T_{sh,i}$ for various pool subcooling, are shown in Fig. 16. The results show that the minimum pool depth linearly increases with the melt superheat, and decreases

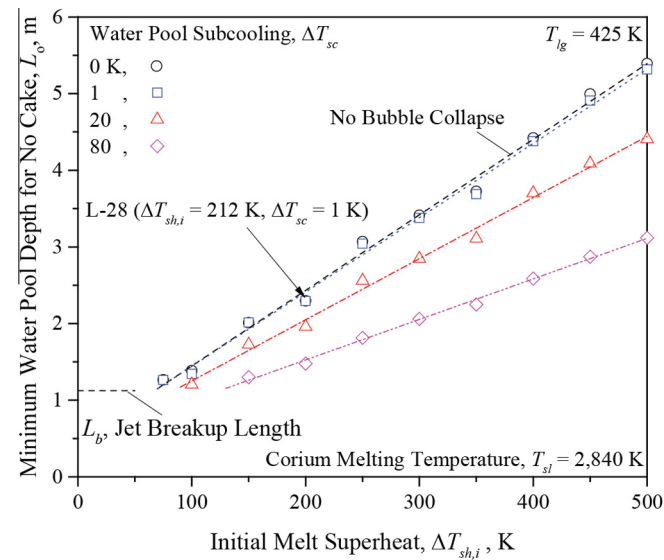


Fig. 16. Predicted minimum water pool depth for no-cake formation, as a function of the initial melt superheat, for the saturation temperature of 425 K (L-28). The results are for several subcooling. The result of L-28 is also shown.

Table 3
Fitting parameters a and b in Eq. (23) for several subcoolings. The adjust- R^2 is also given.

Case	ΔT_{sc}	a	b	Adjust- R^2
L-28	0	0.00986	0.46034	0.9943
	1 (Exp.)	0.0097	0.47088	0.9943
	20	0.00798	0.45252	0.9936
	80	0.00529	0.4666	0.9961
L-31	0	0.0112	0.4642	0.9955
	20	0.00892	0.4796	0.9940
	80	0.00602	0.4864	0.9928
	104 (Exp.)	0.0057	0.4850	0.9938

with liquid subcooling. The predicted results are linear-curve fitted with

$$L_o = a\Delta T_{sh,i} + b, \quad (23)$$

where L_o is the minimum pool depth for no cake formation after the particle transit, and a and b are the fitting parameters. The fitted parameters based on the L-28 and 31 tests are listed in Table 3. The above relation can be as guide in pool depth design for no cake formation (since cake presents a challenging passive cooling problem which can cause degradation of the structure beneath the cake).

5. Conclusion

We developed a hydrodynamic-thermal model, COOLAP code, to describe and predict the fate of melt particles in the gravity-driven transit, sedimentation and cooling in water pool, based on the FARO tests. Eventually, for the may be used assessment of corium coolability under ex-vessel conditions in nuclear power plants. The model considers the following assumptions and scenarios.

- (i) complete breakup of the molten jet in the boiling pool water;
- (ii) radiation-dominated film boiling during particle transit in water forming solid shell around the particles;
- (iii) remelting of the larger particles with sufficient initial melt superheat and formation of cake by liquid-phase sintering, in addition to loose particles; and
- (iv) the cake and loose-particle beds cooling with the boiling heat transfer from the top to the water pool and from the bottom to the wet debris catcher.

We compared the predicted results to two of the FARO [1] tests (namely L-28 and L-31), where complete jet breakup would have occurred and found and concluded the following.

- (a) For the particle-transit period, a view factor of $F = 0.3$ (radiation heat transfer) in film boiling predicts the cake to loose-particle mass fraction, while the spatial/temporal temperature distributions are insensitive to the view factor of $0.1 \leq F \leq 0.3$.
- (b) For the L-28 test, the model predicts a 5/60 ratio for fraction of melt to cake mass, in the liquid-phase sintering, and 10/60 for $F = 0.1$.
- (c) Using the local volume-averaging approach, we predicted the history and temperature distributions of the debris catcher, and cake and loose particle beds for L-28, and loose particle bed for L-31. The predicted temperature at interface between the debris catcher and cake (or loose particle) bed was compared with the experiment [1] with reasonable agreements (considering uncertainties in initial melt superheat, etc.).
- (d) The cake cooling is controlled by the internal heat diffusion (low effective thermal diffusivity) until the cake cools down significantly, so that water can penetrate and significantly enhance cooling by internal evaporation (heat-pipe effect). This is limited to the ending of cooling period.
- (e) The minimum water pool depth is predicted for no cake formation, as functions of the melt initial superheat and water subcooling, showing good agreements with the experimental result. Note that this means the excess depth after the complete breakup of the melt jet and associated with the necessary cooling of melt particles not to cause the cake by the remelting-sintering mechanism. It is important that this can provide technical information on developing an adequate severe accident management guideline (SAMG) to

mitigate the severe accident progression that may threaten the integrity of containment, the final defense-in-depth barrier before the release of radioactive materials to environment and public.

This model will be further developed to continue to investigate the long-term cooling of corium debris bed.

Acknowledgments

This work was financially supported by the National Research Foundation of Korea (NRF) under grants by the Korean Government (MSIP, NRF-2013M2A8A1040987), and by the Department of Mechanical Engineering, Wichita State University, USA.

References

- Bürger, M., 2006. Particulate debris formation by breakup of melt jets: main objectives and solution perspectives. *Nucl. Eng. Des.* 236, 1991–1997. <http://dx.doi.org/10.1016/j.nucengdes.2006.03.032>.
- Bürger, M., Cho, S.H., Berg, E.V., Schatz, A., 1995. Breakup of melt jets as pre-condition for premixing: modeling and experimental verification. *Nucl. Eng. Des.* 155, 215–251. [http://dx.doi.org/10.1016/0029-5493\(94\)00875-Y](http://dx.doi.org/10.1016/0029-5493(94)00875-Y).
- Bürger, M., Buck, M., Pohlner, G., Rahman, S., Kulenovic, R., Fichot, F., Ma, W.M., Miettinen, J., Lindholm, I., Atkhen, K., 2010. Coolability of particulate beds in severe accidents: status and remaining uncertainties. *Prog. Nucl. Energy* 52, 61–75. <http://dx.doi.org/10.1016/j.pnucene.2009.09.015>.
- Chen, X., Luo, R., Yuen, W.W., Theofanous, T.G., 1999. Experimental simulation of microinteractions in large scale explosions. *Nucl. Eng. Des.* 189, 163–178. [http://dx.doi.org/10.1016/S0029-5493\(99\)00032-1](http://dx.doi.org/10.1016/S0029-5493(99)00032-1).
- Cheng, S., Matsuba, K., Isozaki, M., Kamiyama, K., Suzuki, T., Tobita, Y., 2015. A numerical study on local fuel-coolant interactions in a simulated molten fuel pool using the SIMMER-III code. *Ann. Nucl. Energy* 85, 740–752. <http://dx.doi.org/10.1016/j.anucene.2015.06.030>.
- Dombrovsky, L.A., Dinh, T.-N., 2008. The effect of thermal radiation on the solidification dynamics of metal oxide melt droplets. *Nucl. Eng. Des.* 238, 1421–1429. <http://dx.doi.org/10.1016/j.nucengdes.2007.10.010>.
- German, R.M., 1985. *Liquid Phase Sintering*. Plenum Press, New York.
- German, R., Suri, P., Park, S., 2009. Review: liquid phase sintering. *J. Mater. Sci.* 44, 1–39. <http://dx.doi.org/10.1007/s10853-008-3008-0>.
- Kaiser, A., Schuetz, W., Will, H., 2001. PREMIX Experiments PM12-PM18 to investigate the mixing of a hot melt with water.
- Kaviany, M., 1995. *Principles of heat transfer in porous media*. Mechanical Engineering Series., Springer-Verlag, New York.
- Kaviany, M., 2001. *Principles of convective heat transfer*. Mechanical Engineering Series., Springer-Verlag, New York.
- Kaviany, M., 2011. *Essentials of Heat Transfer: Principles, Materials, and Applications*. Cambridge University Press.
- Kim, E., Jung, W.H., Park, J.H., Park, H.S., Moriyama, K., 2016a. Experiments on sedimentation of particles in a water pool with gas inflow. *Nucl. Eng. Technol.* <http://dx.doi.org/10.1016/j.net.2015.12.007>.
- Kim, E., Lee, M., Park, H.S., Moriyama, K., Park, J.H., 2016b. Development of an ex-vessel corium debris bed with two-phase natural convection in a flooded cavity. *Nucl. Eng. Des.* 298, 240–254. <http://dx.doi.org/10.1016/j.nucengdes.2015.12.028>.
- Kondo, S., Konishi, K., Isozaki, M., Imahori, S., Furutani, A., Brear, D.J., 1995. Experimental study on simulated molten jet-coolant interactions. *Nucl. Eng. Des.* 155, 73–84. [http://dx.doi.org/10.1016/0029-5493\(94\)00870-5](http://dx.doi.org/10.1016/0029-5493(94)00870-5).
- Kudinov, P., Karbojian, A., Tran, C.-T., Villanueva, W., 2013. Agglomeration and size distribution of debris in DEFOR-A experiments with Bi₂O₃-WO₃ corium simulatant melt. *Nucl. Eng. Des.* 263, 284–295. <http://dx.doi.org/10.1016/j.nucengdes.2013.06.011>.
- Li, L., Ma, W., 2011. Experimental characterization of the effective particle diameter of a particulate bed packed with multi-diameter spheres. *Nucl. Eng. Des.* 241, 1736–1745. <http://dx.doi.org/10.1016/j.nucengdes.2011.03.013>.
- Lienhard, J.H., 2013. *A Heat Transfer Textbook*. Courier Corporation.
- Lipinski, R.J., 1984. A coolability model for postaccident nuclear reactor debris. *Nucl. Technol.* 65, 53–66.
- Liu, C., Theofanous, T.G., 1995. Film boiling on spheres in single-and two-phase flows. Part I: experimental studies. In: *ANS Proceedings of the National Heat Transfer Conference, Portland, US*, pp. 34–47.
- Liu, C., Theofanous, T.G., 1996. Film boiling on spheres in single- and two-phase flows. DOE/ER/12933-3, DOE/ID-10499.
- Magallon, D., 2006. Characteristics of corium debris bed generated in large-scale fuel-coolant interaction experiments. *Nucl. Eng. Des.* 236, 1998–2009. <http://dx.doi.org/10.1016/j.nucengdes.2006.03.038>.
- Matsuo, E., Abe, Y., Chitose, K., Koyama, K., Itoh, K., 2008. Study on jet breakup behavior at core disruptive accident for fast breeder reactor. *Nucl. Eng. Des.* 238, 1996–2004. <http://dx.doi.org/10.1016/j.nucengdes.2007.11.011>.
- Moriyama, K., Park, H.S., 2015. Probability distribution of ex-vessel steam explosion loads considering influences of water level and trigger timing. *Nucl. Eng. Des.* 293, 292–303. <http://dx.doi.org/10.1016/j.nucengdes.2015.07.062>.
- Moriyama, K., Park, H.S., 2016. Simulation of melt jet breakup experiments by JASMINE with an empirical correlation for melt particle size distribution. *J. Nucl. Sci. Technol.*, 1–14.
- Moriyama, K., Maruyama, Y., Usami, T., Nakamura, H., 2005. Coarse break-up of a stream of oxide and steel melt in a water pool, JAERI-Research 2005–017, Japan Atomic Energy Research Institute.
- Moriyama, K., Park, H.S., Kim, M.H., 2015. Simulation of melt jet breakup and cooling in a water pool with an empirical correlation for melt particle size distribution. In: *ICONE23: 23rd International Conference on Nuclear Engineering*. Makuhari, Japan, pp. ICONE23-1672.
- Munson, B.R., Rothmayer, A.P., Okiishi, T.H., 2012. *Fundamentals of Fluid Mechanics*, seventh ed. John Wiley and Sons Inc.
- Nukiyama, S., 1966. The maximum and minimum values of the heat Q transmitted from metal to boiling water under atmospheric pressure. *Int. J. Heat Mass Transfer* 9, 1419–1433. [http://dx.doi.org/10.1016/0017-9310\(66\)90138-4](http://dx.doi.org/10.1016/0017-9310(66)90138-4).
- Oliveira, A.A.M., Kaviany, M., 1999. Role of inter-and intraparticle diffusion in nonuniform particle size gasless compacted-powder combustion synthesis—I: formulation. *Int. J. Heat Mass Transfer* 42, 1059–1073.
- Poulikakos, D., 1994. *Conduction Heat Transfer*. Prentice Hall.
- Rogers, J.A., Kaviany, M., 1992. Funicular and evaporation-front regimes in convective drying of granular beds. *Int. J. Heat Mass Transfer* 35, 469–480.
- Saito, R., Abe, Y., Yoshida, H., 2016. Breakup and fragmentation behavior of molten material jet in multi-channel of BWR lower plenum. *J. Nucl. Sci. Technol.* 53, 147–160. <http://dx.doi.org/10.1080/00223131.2015.1027756>.
- Salikhov, T.P., Kan, V.V., Ronchi, C., 1999. Radiative properties of uranium dioxide near its melting point. *Int. J. Thermophys.* 20, 1163–1176. <http://dx.doi.org/10.1023/A:1022615222797>.
- Schneider, P.J., 1985. *Conduction Heat Transfer, Handbook of Heat Transfer Fundamentals*. McGraw-Hill, New York.
- Song, J.H., Suh, N.D., 2009. An evolution of molten core cooling strategies. *Nucl. Eng. Des.* 239, 1338–1344. <http://dx.doi.org/10.1016/j.nucengdes.2009.02.010>.
- Spencer, B.W., Wang, K., Blomquist, C.A., McUmber, L.M., Schneider, J.P., 1994. Fragmentation and quench behavior of corium melt streams in water. <http://dx.doi.org/10.2172/10136350>.
- Udell, K.S., 1985. Heat transfer in porous media considering phase change and capillarity—the heat pipe effect. *Int. J. Heat Mass Transfer* 28, 485–495.
- Uršič, M., Leskova, M., Mavko, B., 2011. Improved solidification influence modelling for Eulerian fuel-coolant interaction codes. *Nucl. Eng. Des.* 241, 1206–1216. <http://dx.doi.org/10.1016/j.nucengdes.2010.05.001>.
- Vakarelski, I.U., Chan, D.Y.C., Thoroddsen, S.T., 2014. Leidenfrost vapour layer moderation of the drag crisis and trajectories of superhydrophobic and hydrophilic spheres falling in water. *Soft Matter*.
- Voller, V., Cross, M., 1981. Accurate solutions of moving boundary problems using the enthalpy method. *Int. J. Heat Mass Transfer* 24, 545–556. [http://dx.doi.org/10.1016/0017-9310\(81\)90062-4](http://dx.doi.org/10.1016/0017-9310(81)90062-4).